Bio-Inspired Band-Gap Tunable Elastic Optical Multilayer Fibers

Submitted to ADVANCED MATERIALS

DOI: 10.1002/adma.((please insert DOI)

Bio-inspired band-gap tunable elastic optical multilayer fibers

By *Mathias Kolle*[1]*, *Alfred Lethbridge*[2], *Moritz Kreysing*[3], *Jeremy J. Baumberg*[4], *Joanna Aizenberg*[1], and *Peter Vukusic*[2]*

[1] Dr. Mathias Kolle, Prof. Joanna Aizenberg
Harvard University, School of Engineering and Applied Sciences
9 Oxford Street, Cambridge, MA-02138 (US)
E-mail: mkolle@seas.harvard.edu

[2] Prof. Peter Vukusic, Alfred Lethbridge
University of Exeter, School of Physics
Stocker Road, Exeter, EX4 4QL (UK)
E-mail: P.Vukusic@exeter.ac.uk

[3] Dr. Moritz Kreysing
Ludwig Maximilians University, Systems Biophysics, Department of Physics
Amalienstr. 54, München, D-80799 (GER)

[4] Prof. Jeremy J. Baumberg
University of Cambridge, Nanophotonics Centre, Cavendish Laboratory
JJ Thompson Ave, Cambridge, CB3 0HE (UK)

Keywords: (Biophotonics, Biooptics, Photonic Fibers, Cylindrical Bragg Fibers, Bandgap-tuning)

Knowledge of the interplay between the morphology, composition and optical appearance of biological photonic systems can provide broad inspiration for novel artificial photonic elements.[1-3] On occasion, the study of natural photonics yields specific design templates for optical technologies.[4-9] To this end, we present the results of the investigation of the hierarchical photonic structure discovered in the seed coat of *Margaritaria nobilis* fruits, which directly inspired our creation of novel photonic fibers. The fruit's hue results from the interference of light within a concentrically-layered architecture found inside individual cells in the seed's outer tissue layers. The natural structure presents two codependent, technologically exploitable features for light and color manipulation: regularity on the nanoscale that is superposed with microscale cylindrical symmetry, resulting in wavelength

selective scattering of light in a wide range of directions. This is the foundation for novel soft bio-inspired photonic fibers with the spectral filtering capabilities and color brilliance of a planar Bragg stack compounded with a large angular scattering range introduced by the microscale curvature, which also decreases the strong directional chromaticity variation usually associated with flat multilayer reflectors. Transparent and elastic synthetic materials equip the multilayer interference fibers with high reflectance that is dynamically tuned by longitudinal mechanical strain. A two-fold elongation of the elastic fibers results in a shift of reflection peak center wavelength of over 200nm. The bio-inspired design and manufacture of this form of soft photonic fiber heralds the transition to novel fiber-based flexible photonic materials and textiles with colors that are tunable over the entire visible spectrum and optical strain sensors.

Nature's most vivid colors, highest transparencies, strongest whites and deepest blacks rely on ordered, quasi-ordered or disordered structures with lattice constants or scattering element sizes on the order of the wavelength of visible radiation.[10-16] By inducing interference or diffraction, biological photonic structures of a wide structural diversity strongly alter the spectral composition of reflected and transmitted light resulting in the stunning structural colors of many organisms.[17,18] One-dimensional multilayer arrangements play an important role in the creation of structural colors in nature and have primarily been studied in the animal kingdom, especially the insect world.[10,19,20] Planar layered photonic system have recently also been increasingly frequently reported in various plants.[21-24]

The fruits of the plant *Margaritaria nobilis* in the rain forests of Middle and South America have a striking blue - green hue **(Fig. 1a)**. The plant partly relies on seed dispersal by birds which might be attracted by the colorful display.[25,26] The cells in the fruit's blue seed coat are elongated and mostly appear blue or green (Fig. 1a, b). Several layers of cells are stacked on

top of each other with varying planar orientation of the individual cell layers (Fig. 1c). A single cell cross-section reveals that the entire interior volume is occupied by a periodic concentrically-layered morphology with an overall periodicity of (180 ± 30) nm (Fig. 1d, e). Light incident on the fruit's surface undergoes interference within the periodic structure in each cell resulting in the reflection of blue light.

Under directional illumination a planar multilayer interference structure can only display its bright coloration in the specular reflection direction. The hue of such planar Bragg stacks strongly depends on the angle of incidence. Under diffuse illumination the observed color blue-shifts for increasing observation angle. By contrast, in *M. nobilis* fruits the superposition of a microscopic curvature on the nanoscale regularity of the layered structure within each individual seed coat tissue cell combined with the fruit's overall macroscopic curvature leads to an increased visibility of the reflected structural color across a wide angular range. Under directional illumination, a part of the curved multilayer in a majority of the individual cells is oriented to satisfy the specular reflection condition providing a spatially varying pixelated sparkle of different hues (Fig. 1a) that depend on the locally varying angle of light incidence. In diffuse light this sparkle is suppressed as the light reflected by each fruit cell towards the observer originates from light incident on the fruit from various directions, producing a more isotropic color that only gradually changes across the fruit due to the macroscopic curvature.

The emergence of unique structural and optical properties from combinations of structures on different length scales within hierarchical synergistic assemblies is a principle often encountered when studying natural systems.[19,27] Increasingly frequently this concept is also applied in novel optical technologies.[6,7,9] The hierarchical photonic architecture in the seed coat of the *M. nobilis* fruit is the key element involved in the creation of intense blue and green hues. It provides inspiration for the manufacture of artificial photonic fibers with the

optical functionality being defined by the interplay of nanoscopic regularity and superimposed microscopic curvature. The artificial bio-inspired system presented in this article consists of concentric multilayer-wrapped fibers with a radially periodic refractive index profile built from only two alternating phases. While similar to its natural model in dimensions and underlying optical interactions, the artificial system avoids many of the complexities in the natural structure including the ellipticity of the fruit cells' cross-section and any existing fine structure within the periodic layers.

Optical fiber systems with multilayer claddings have theoretically been discussed since the late 70's and have more recently been manufactured using standard fiber drawing processes from macroscopic preforms.[28-32] The choice of materials that can be drawn into multilayer fibers is constrained to a limited, albeit continuously expanding set of components.[33] In particular, the preform material combinations need to provide an appropriate refractive index contrast and have matching thermal expansion coefficients in order to prevent fracturing at the material interfaces during the processing at elevated temperature.[33]

Here, we present an alternative approach that allows fabrication of fibers at room temperature from a wide range of soft organic and also inorganic materials with varying optical and mechanical properties that are not restricted to a translational symmetry along the fiber axis as in thermally drawn fibers. The fibers reported in this article consist of two elastomeric dielectrics, polydimethylsiloxane (PDMS) and polyisoprene-polystyrene triblock copolymer (PSPI), two inexpensive materials that are commercially available in industrial quantities and provide a sufficiently high refractive index contrast ($n_{PDMS} = 1.41 \pm 0.02$, $n_{PSPI} = 1.54 \pm 0.02$, determined by ellipsometry). Multilayer fibers are produced by initially forming a bilayer of the two constituent materials, which is subsequently rolled up onto a thin glass fiber (≈ 10 - 20μm diameter) to form the multilayer cladding (Fig. 1f and **Fig. S1** in supp. inf.).[34,35]

This material system, which was reported earlier in the context of planar flexible multilayer systems,[34] was chosen here for its advantageous set of properties for the controlled tuning of the fiber's optical performance, which is demonstrated below. The fiber rolling technique used to produce the fibers has previously been employed for the creation of multilayer claddings on rods with macroscopic diameter to facilitate the manufacture of microscopically planar multilayer stacks. Here, we show for the first time that this technique can be employed to form concentric multilayers on core fibers of only ~15µm diameter using elastic materials. Such multilayer fibers with curvature on the microscale display optical properties that are distinctly different from the macroscopic rolls previously produced.[35]

Other dielectric materials that have been used in the fiber manufacture include thermoplastics, for instance polystyrene and poly(methyl methacrylate). Thin metal films have been incorporated in non-stretchable fibers with macroscale diameter employing the rolling technique.[35] Spray coating or blade coating, two industrially well-established techniques that are compatible with roll-to-roll processing, could be explored as viable alternatives for the bilayer production on a larger scale.

The individual thicknesses of the two films in the initial bilayer can be tuned during the film deposition. Consequently, the spectral position of the reflection band of the fibers can be freely adjusted. Three fibers with high reflectivity in different color ranges and the corresponding complementary color in transmission are shown in Fig. 1g. Scanning electron micrograph images of the cross-section of a green fiber visualize the concentric multilayer cladding with 80 periods wrapped around the core glass fiber (Fig.1h, i).

Similar to the optical signature of the tropical fruit (**Fig. 2**a, b), these fibers show a pronounced reflection in a finite wavelength range imposed by the multilayer periodicity (Fig. 2d, e) and a corresponding drop in transmission (Fig. 2f, g). Fibers rolled with multilayer claddings of up to 150 periods provide a reflectivity of more than 90% in their reflection band and a bandwidth varying from 70nm to 30nm, decreasing with increasing number of layers in the cladding.

Collection of spectra along a line perpendicular to the fruit cell axis (white solid line in Fig. 2a) allows for the reconstruction of the axially symmetric spatial reflection intensity distribution (Fig. 2c). This measurement was also performed on the fibers to determine their reflection and transmission intensity distribution. Note that due to its curvature, the concentric multilayer reflector translates the lateral distance from the fiber's symmetry axis at which each spectrum was taken into a corresponding incident angle (**Fig. 3**a, b). This allows for the direct measurement of the dispersion relation of the multilayer fiber system in reflection and transmission (Fig. 3c, d, for details see **Fig. S2** and discussion in supp. inf.).

Under directional illumination the difference in radial variation of the peak wavelength from fiber and individual fruit cells results from a subtle difference in geometry. Cross-sections of the fruit cells show that the multilayer is arranged in concentric ellipses aligned with the major axis in the plane of the fruit's surface which leads to a less pronounced color variation across a single cell. In contrast, the multilayer cladding of the artificial fibers has a circular concentric cross-section inducing a radial color variation with larger gradient.

Finite Difference Time Domain (FDTD) simulations of the fibers' optical performance were carried out on a high performance computing cluster using the MIT Electromagnetic Equation Propagation software package (MEEP)[36] to explain the complexity of the measured

dispersion diagrams and to predict the change in optical properties due to a variation in the fiber design. This approach was motivated by the recent investigation of a photonic structure in a fish retina, where FDTD simulations of the interaction of light with the complex hierarchical biological photonic system could provide valuable insight into the interplay of all components on the different length scales.[37] The simulations presented here result from interactions of light with a fiber of 60 layers with 340nm periodicity in the outer multilayer cladding zone matching the geometry of the blue fiber from which the experimental dispersion diagrams were obtained. The inner cladding zone adjacent to the fiber core was occupied by a small number of bilayers of ≈710nm periodicity also found in the real fiber. In the simulations the spatiotemporal electromagnetic field amplitude distributions of light reflected and transmitted by the fiber are collected in the fiber's near-field after excitation with a broadband pulse. An appropriate far-field transformation yields the reflected intensities as a function of frequency or photon energy and wave vector component k_x - i.e. the dispersion relation of the multilayer fibres.[38,39]. The band structures obtained in these simulations (Fig. 3f, g) match the experimentally acquired dispersion diagrams of the fibers (Fig. 3c, d). The main Bragg reflection peak at a photon energy of 2.5eV (corresponding to a wavelength of 496nm) and its spectral variation with propagation direction is captured in both sets of data for transmission and reflection. A blue-shift of the reflection band is observed with increasing propagation angle in experiment and simulation. However, this spectral variation amounts to less than 40% of the blue-shift expected from a comparable flat multilayer structure, showing that the curvature of the multilayer cladding more than halves the angular variation in chromaticity usually associated with multilayer reflectors. The same effect arises for reflection of light from the multilayered cells in the seed coat of the *M. nobilis* fruit (Fig. 3c) explaining its isotropic coloration in diffuse illumination.

In this particular fiber sample, the splitting in the reflection band observed in experiment and simulation is caused by interference of light in the inner zone of the multilayer cladding with ≈710nm periodicity surrounding the fiber core. High frequency intensity fluctuations as a function of photon energy in the simulations are caused by the fiber core, which acts as a larger resonant cavity introducing an abundance of defect modes. This is not captured in the experimental data due to a limited spectral resolution. In fiber designs with smaller cores these cavity modes would be detectable and potentially even be manifested in angle-dependent spectrally varying intensity fluctuations visible to the naked eye. Some of the light propagating transversely through the fiber experiences guiding within the individual layers resulting in additional weak modes seen at photon energies between 1.7 - 2.4eV captured in simulations and experiments. These modes only occur for light polarized in the fiber's axial direction (see **Fig. S3** in supp. inf.). A detailed investigation of this effect is beyond the scope of this paper and will be addressed elsewhere.

The glass fiber that acts as the substrate for the multilayers in the rolling process can be removed from the fiber by dissolution in hydrofluoric acid or by simply pulling it out of the multilayer cladding. Once the glass core is removed, the fiber, being composed of two elastomers, can be elastically deformed by stretching it along its axis. An elongation along the fiber axis leads to a compression perpendicular to it, causing a decrease of its overall diameter and a reduction of the thickness of each individual layer. Due to the comparable Poisson's ratio of the constituent elastic materials the thickness ratio and the reflection intensity remain constant while the reflection band blue-shifts. This way, the reflected and transmitted color can be reversibly tuned by axial extension of the fibers (**Fig. 4a**, d). A reversible peak wavelength shift of over 200nm has been recorded for axial elongations of a fiber to over 200% of its original length (Fig. 4b, c).

From Poisson's ratio and the proportionality between the thickness of individual layers in the cladding and the spectral band-gap position, the reflection peak center wavelength λ_{Peak} is predicted to follow the relation $\lambda_{\mathrm{peak}} = \lambda^0_{\mathrm{peak}}\,(1+\mathcal{E})^{-\nu}$, where $\lambda^0_{\mathrm{peak}}$ represents the reflection peak centre wavelength at zero axial strain, $\mathcal{E}$ the applied axial strain and ν the fibre's Poisson's ratio. Fitting the experimental data with this relation yields a Poisson's ratio of $\nu = 0.46 \pm 0.02$ for the stretchable multilayer fibers matching the Poisson's ratios of the constituent rubber materials (Fig. 4c). This is in good agreement with results obtained earlier for the deformation of planar elastic multilayers.[34]

In this paper, we have given an example of the versatility of bio-inspired approaches for the manufacture of novel photonic elements. The hierarchical photonic architecture in individual cells of the fruits of the tropical plant *Margaritaria nobilis* served as a model for the creation of novel tunable band-gap multilayer fibers with a large tuning range in the visible spectrum. Our room temperature fiber rolling technique allows fabrication of multilayer fibers with hundreds of layers from a wide range of polymeric material combinations that would not be realizable by conventional thermal fiber drawing. The fibers' band-gap center frequency can initially be tuned by adjusting the individual film thicknesses of the two constituent layers prior to the rolling process, which also allows shifting of the fibers' tuning range into the near UV or near IR. Chirped multilayer fibers can be realized by applying an appropriate force on the elastic bilayer during rolling of the multilayer cladding (see Fig. S1 in the supp. inf.).

The incorporation of gold or silver layers into the concentric multilayer offers potential for the development of novel micron-scale fiber-based meta-materials. Asymmetric structures or chirality could be incorporated into the fibers by patterning of the initial bilayer prior to the rolling, promising additional interesting optical properties.[40] Removal of the fiber core from inside the multilayer cladding permits mechanical deformation of fibers to more than twice their original length, which causes a tuning of the band-gap and a spectral blue-shift of over

200nm. In the future, the incorporation of flexible core fibers will render the removal step obsolete. The flexibility in the choice of constituent materials for the multilayer fibers and their unique combination of mechanical and optical properties holds great potential for applications in mechanically tunable light guides or optical strain sensing. The fibers' mechanical flexibility and elasticity, in addition to the demonstrated color brilliance and tunability, can make them a versatile novel material for smart, color-dynamic textiles. The reported multilayer fiber manufacturing process can in principle be applied to a wide range of synthetic materials with varying optical and mechanical properties. Large area deposition of the initial bilayer can be achieved by spraying or blade coating in a roll-to-roll process before final rolling of the multilayer fibers. Hollow photonic fibers providing good thermal insulation can be produced by employing hollow polymeric micro-tubing as the inner fiber core. Exposure of the fibers to different solvents in the vapor or liquid phase would result in varying degrees of swelling and a corresponding reflection peak red-shift endowing the fibers or textiles made thereof with optical solvent sensing capacities. The final formation of the multilayer rolls could in principle also be achieved by self-induced rolling of the bilayer caused by directional stresses, which can be induced by gradually swelling one of the bilayer phases selectively.[41]

Experimental Section

Fiber manufacture

A thin polydimethylsiloxane (PDMS, Sylgard 184, Dow Corning) film was spun from a 4%wt solution in heptane onto a sacrificial water-soluble polystyrene-sulfonic acid layer on a silicon wafer. The PDMS film was cross-linked by curing it on a hotplate for 2h at 70ºC. Subsequently, a bilayer was formed by spin-coating a polystyrene-polyisoprene-polystyrene triblock copolymer (PSPI, Sigma Aldrich, 14%wt content polystyrene) film on top of the cross-linked PDMS layer from a 4%wt solution in toluene (Fig. 1f left). Stripes of 12cm by 1-

2cm of the bilayer were then released from the wafer onto the surface of a water bath. This was achieved by immersing the sample slowly into the water at an angle varying between 30-45º allowing the water to dissolve the sacrificial water-soluble film between the elastomer bilayer and the substrate, thereby detaching the bilayer from the substrate. A thin glass fiber (10-20µm diameter) was then lowered onto the end of the floating bilayer, where it adhered to the PSPI film, the top layer in the bilayer. Once the core glass fiber had attached it was rotated at a speed of 10-20 turns per minute rolling up the bilayer to form the multilayer cladding (Fig. 1f right) [34,35].

Structural and optical analysis

Images of the cross-sections of the fruit's seed coat tissue cells were obtained by scanning electron microscopy (Hitachi S-3200N SEM). For imaging, the samples were coated with a 3nm thick film of a gold/palladium alloy. The cells internal periodic structure was visualized by transmission electron microscopy (JEOL 100S TEM). Images were acquired after fixing and staining samples according to the protocol described elsewhere [42]. Cross-sections of the fibers were obtained by cryo-fracture. Fractured fibers were coated with a 3-5nm thick platinum film to avoid charging artifacts during imaging and visualized using a field emission scanning electron microscope (Zeiss Supra55VP).

Simultaneous imaging and micro-spectroscopic spatial reflection / transmission intensity mapping of the fruit's surface and the fibers was performed in a modified optical microscope (Leica DMRX). The samples were illuminated in the area of interest with a halogen lamp in reflection or transmission. Via an additional microscope port, a fraction of the reflected light was collected confocally and guided by a fiber to a spectrometer (Maya 2000 Pro, Ocean Optics). The detection spot size depends on the diameter of the fiber and the magnification of the objective lens. Measurements with a 50x objective (NA = 0.55) and a fiber with 50µm

core diameter resulted in a spatial resolution of 1μm. All spectra are referenced against a flat silver mirror of ≥95% reflectance in the wavelength range of 400-800nm. In order to acquire spatially and spectrally resolved intensity distributions of a specific area on a sample, the sample was translated step-wise in the focal plane of the microscope with a minimum step size of 1μm using an automated, remote-controlled stage (Prior ES110). Individual spectra were acquired after each scanning step resulting in a complete map of the spectrally-resolved intensity distribution of the samples in reflection or transmission.

Optical modeling

The transverse reflection and transmission of cylindrical multilayer fibers was modeled using the MIT Electromagnetic Equation Propagation package (MEEP) [36] interfaced with custom-made C++ code to feed MEEP with the refractive index distributions in the simulation cell and to deduce the dispersion relations from the simulated field distributions. The fiber was modeled in cross-section with the layer thicknesses and the core fiber diameter acquired from the scanning electron microscope images of fiber cross-sections (d_{PDMS} = 240nm, d_{PSPI} = 100nm, d_{core} = 14μm, Fig. 1h, i) and refractive indices of the constituent materials measured by ellipsometry (n_{PDMS} =1.41 n_{PSPI} = 1.54, n_{core} = 1.5). The modeling cell was bordered by absorbing boundaries simulating the effect of a finite numerical aperture of the microscope objective. A light pulse containing light of wavelengths 300 - 900nm was propagated through the simulation cell. Detectors positioned above and below the fiber captured the electromagnetic fields as a function of time and space. The distance of the detectors to the fiber was chosen in order to detect waves propagating in an angular range that is commensurate with the numerical aperture of the microscope objective in the experiments. The detected fields served to deduce the reflection and transmission dispersion diagrams of the fibers using a suitable Fourier transformation algorithm to perform the far-field transformation and the spectral analysis. The simulations were repeated with periodic

boundary conditions to ensure that no artifact spatial frequencies result from the absorbing boundaries and to ensure that conservation of energy was observed in the simulations (i.e reflection and transmission add up to unity).

Acknowledgements

The authors thank Dr. Silvia Vignolini and Dr. Beverly J. Glover for their helpful comments on the manuscript and Stuart Blackman for kindly providing some *M. nobilis* fruit samples to start the investigation. Financial support from the US Air Force Office of Scientific Research Multidisciplinary University Research Initiative under award numbers FA9550-09-1-0669-DOD35CAP, FA9550-10-1-0020 and the UK Engineering and Physical Sciences Research Council EP/G060649/1 is gratefully acknowledged. M.Ko. acknowledges the financial support from the Alexander von Humboldt Foundation in form of a Feodor Lynen postdoctoral research fellowship. This work was performed in part at the Center for Nanoscale Systems (CNS), a member of the National Nanotechnology Infrastructure Network (NNIN), which is supported by the National Science Foundation under NSF award no. ECS-0335765. CNS is part of Harvard University. Supporting Information is available online from Wiley InterScience or from the author.

Received: ((will be filled in by the editorial staff))
Revised: ((will be filled in by the editorial staff))
Published online: ((will be filled in by the editorial staff))

[1] L. Lee, R. Szema, *Science* **2005,** *310*, 1148.

[2] A. Parker, H. Townley, *Nat. Nanotechnol.* **2007**, *2*, 347.

[3] L. P. Biró, J. P. Vigneron, *Laser Photonics Rev.* **2011**, *4*, 27.

[4] J. P. Vigneron, M. Rassart, C. Vandenbem, V. Lousse, O. Deparis, L. P. Biró, D. Dedouaire, A. Cornet, P. Defrance, *Phys. Rev. E* **2006**, *73*, 041905.

[5] R. Potyrailo, H. Ghiradella, A. Vertiatchikh, K. Dovidenko, J. R. Cournoyer, E. Olson, *Nat. Photonics* **2007**, *1*, 123.

[6] B. T. Hallam, A. G. Hiorns, P. Vukusic, *Appl. Opt.* **2009**, *48*, 3243.

[7] M. Kolle, P. M. Salgard-Cunha, M. R. J. Scherer, F. Huang, P. Vukusic, S. Mahajan, J. J. Baumberg, U. Steiner, *Nat. Nanotechnol.* **2010**, *5*, 511.

[8] A. D. Pris, Y. Utturkar, C. Surman, W. G. Morris, A. Vert, S. Zalyubovskiy, T. Deng, H. T. Ghiradella, R. A. Potyrailo, *Nat. Photonics* **2012**, *6*, 195.

[9] K. Chung, S. Yu, C.-J. Heo, J. W. Shim, S.-M. Yang, M. G. Han H.-S. Lee and Y. Jin, S. Y. Lee, N. Park, J. H. Shin, *Adv. Mater.* **2012**, *24*, 2375.

[10] M. F. Land, *Prog. Biophys. Mol. Bio.* **1972**, *24*, 75.

[11] S. Kinoshita, S. Yoshioka, J. Miyazaki, *Rep. Prog. Phys.* **2008**, *71*, 076401.

[12] R. O. Prum, R. Torres, *J. Exp. Biol.* **2003**, *206*, 2409.

[13] M. F. Land, D. E. Nilsson, *Animal Eyes*, Oxford University Press, Oxford, UK **2001**.

[14] A. Yoshida, M. Motoyama, A. Kosaku, K. Miyamoto, *Zool. Sci.* **1997**, *14*, 737.

[15] P. Vukusic, B. Hallam, J. Noyes, *Science* **2007**, *315*, 348.

[16] P. Vukusic, J. R. Sambles, C. R. Lawrence, *Proc. R. Soc. London, Ser. B* **2004**, *271*, S237.

[17] A. R. Parker, *J. Opt. A: Pure Appl. Opt.* **2000**, *2*, R15.

[18] P. Vukusic, J. R. Sambles, *Nature* **2003**, *424*, 852.

[19] S. Kinoshita, S. Yoshioka, *ChemPhysChem* **2005**, *6*, 1442.

[20] P. Vukusic, R. J. Wootton, J. R. Sambles, *Proc. R. Soc. London, Ser. B* **2004**, *271*, 595.

[21] D. W. Lee, J. B. Lowry, *Nature* **1975**, *254*, 50.

[22] D. W. Lee, *Am. Sci.* **1997**, *85*, 56.

[23] K. R. Thomas, M. Kolle, H. M. Whitney, B. J. Glover, U. Steiner, *J. R. Soc., Interface* **2010**, *7*, 1699.

[24] S. Vignolini, P. J. Rudall, A. V. Rowland, A. Reed, E. Moyroud, R. B. Faden, J. J. Baumberg, B. J. Glover, U. Steiner, *Proc. Natl. Acad. Sci. U. S. A.* **2012**, *109*, 15712.

[25] M. Galetti, in *Seed Dispersal and Frugivory: Ecology, Evolution, and Conservation* (Eds. D. J. Levey, W. R. Silva, M. Galetti), CABI Publishing, New York, USA **2002**, Ch. 12.

[26] E. Cazetta, L. S. Zumstein, T. A. Melo-Júnior, M. Galetti, *Rev. Bras. Bot.* **2008**, *31*, 303.

[27] J. Aizenberg, J. C. Weaver, M. S. Thanawala, V. C. Sundar, D. E. Morse, P. Fratzl, *Science* **2005**, *309*, 275.

[28] P. Yeh, A. Yarif, *J. Opt. Soc. Am.* **1978**, *68*, 1196.

[29] S. Hart, G. R. Maskaly, B. Temelkuran, P. H. Prideaux, J. D. Joannopoulos, Y. Fink, *Science* **2002**, *296*, 510.

[30] B. Temelkuran, S. Hart, G. Benoit, J. Joannopoulos, Y. Fink, *Nature* **2002**, *420*, 650.

[31] J. Knight, *Nature* **2003**, *424*, 847.

[32] B. Gauvreau, N. Guo, K. Schicker, K. Stoeffler, F. Boismenu, A. Ajji, R. Wingfield, C. Dubois, M. Skorobogatiy, *Opt. Express* **2008**, *16*, 15677.

[33] A. F. Abouraddy, M. Bayindir, G. Benoit, S. D. Hart, K. Kuriki, N. Orf, O. Shapira, F. Sorin, B. Temelkuran, Y. Fink, *Nat. Mater.* **2007**, *6*, 336.

[34] M. Kolle, B. Zheng, N. Gibbons, J. J. Baumberg, U. Steiner, *Opt. Express* **2010**, *18*, 4356.

[35] N. Gibbons, J. J. Baumberg, C. Bower, M. Kolle, U. Steiner, *Adv. Mater.* **2009**, *21*, 3933.

[36] A. F. Oskooi, D. Roundy, M. Ibanescu, P. Bermel, J. D. Joannopoulos, S. G. Johnson, *Comput. Phys. Commun.* **2010**, *181*, 687.

[37] M. Kreysing, R. Pusch, D. Haverkate, M. Landsberger, J. Engelmann, J. Gentsch, C. Mora-Ferrer, E. Ulbricht, J. Grosche, K. Franze, S. Streif, S. Schumacher, F. Makarov, J.

Guck, H. Wolburg, J. Bowmaker, G. von der Emde, S. Schuster, H.-J. Wagner, A. Reichenbach, M. Francke, *Science* **2012**, *336*, 1700.

[38] M. Born, E. Wolf, *Principles of Optics,* Cambridge University Press, Cambridge, UK **2005**.

[39] J.W. Goodman, *Introduction to Fourier Optics*, Roberts and Company Publishers, Greenwood Village, USA, **2005**.

[40] F. M. Huang, J. K. Sinha, N. Gibbons, P. N. Bartlett, J. J. Baumberg, *Appl. Phys. Lett.* **2012**, *100*, 193107.

[41] V. Luchnikov, L. lonov, M. Stamm, *Macromol. Rapid Commun.* **2011**, *32*, 1943.

[42] P. Vukusic, R. Kelly, I. Hooper, *J. R. Soc., Interface* **2008**, *6*, Suppl.2, S193.

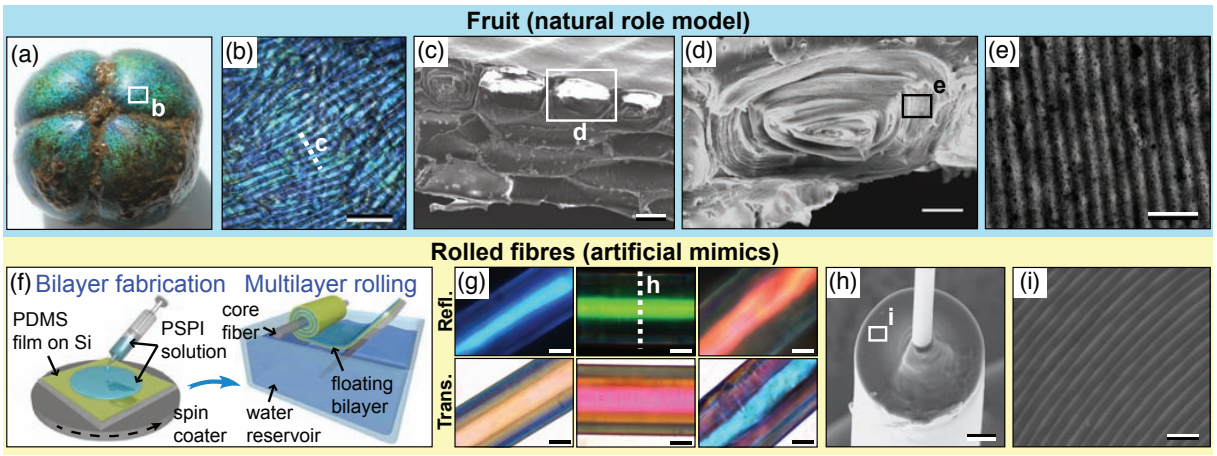

Figure 1: Fruit and fibers. (a) A *Margaritaria nobilis* fruit without its capsule (~10mm in diameter). (b) Optical micrograph of the fruit's surface showing the elongated blue cells. (c) A scanning electron micrograph of a cross-section through the outer layers of the fruit's endocarp is showing several stacks of cells. (d) A cross-section through a single tissue cell reveals the interior architecture - a concentric, flattened cylindrical layered structure. (e) A section of the layered architecture within a single cell visualized by transmission electron microscopy. (f) Schematic representation of the manufacturing of artificial photonic fibers. (g) Optical micrographs of three rolled-up multilayer fibers with different layer thicknesses and colors in reflection (top) and transmission (bottom). (h) Scanning electron micrograph of a fiber cross-section showing the multilayer cladding wrapped around the fiber's glass core. (i) Scanning electron micrograph of the individual layers in the cladding. Scale bars: 200µm (b), 20µm (c), 10µm (d), 500nm (e), 20µm (g), 20µm (h) and 1µm (i).

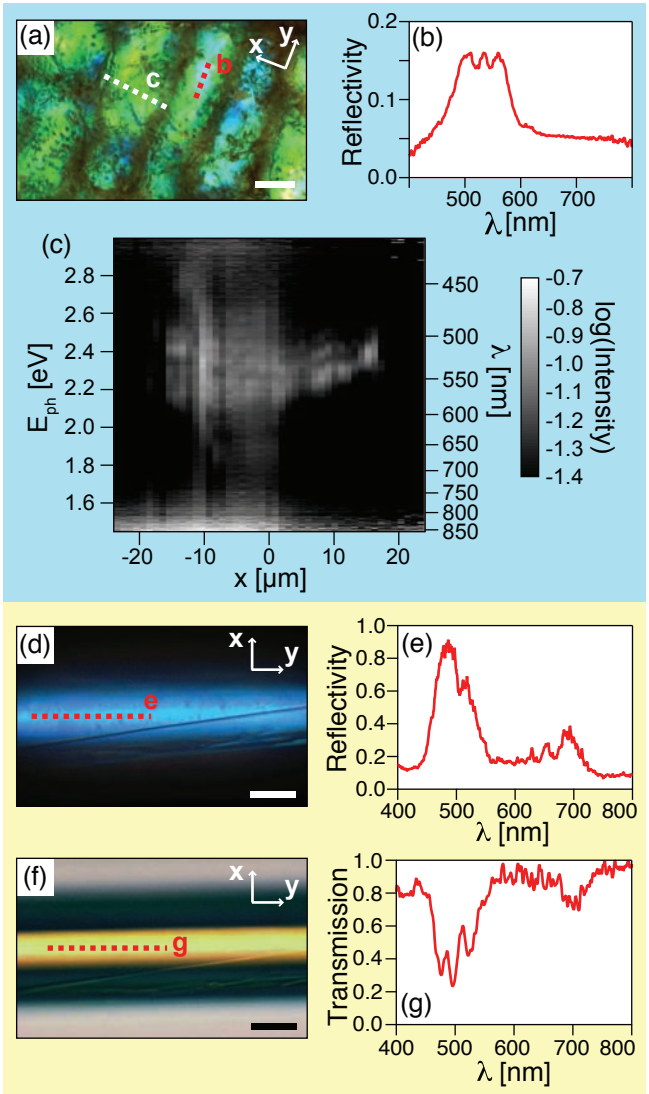

Figure 2: Optical characterization of the fruit and the fibers. (a) Optical micrograph of a fruit's surface visualizing parts of elongated tissue cells. (b) The corresponding reflection spectrum averaged along the red dashed line in (a). (c) Spectrally resolved intensity distribution acquired from a line scan (white line in (a)) radially across a single cell showing the variation of the reflection band induced by the curvature of the layered nanoscale architecture. E_{ph} - photon energy, x - spatial position radially along the fiber, centered at the fiber axis. (d) Optical micrograph of a blue fiber in reflection. (e) The corresponding reflection spectrum averaged along the red dashed line in (c). (f) Optical image of the same fiber in transmission. (g) The corresponding transmission spectrum averaged along the red dashed line in (e). All scale bars – 20µm.

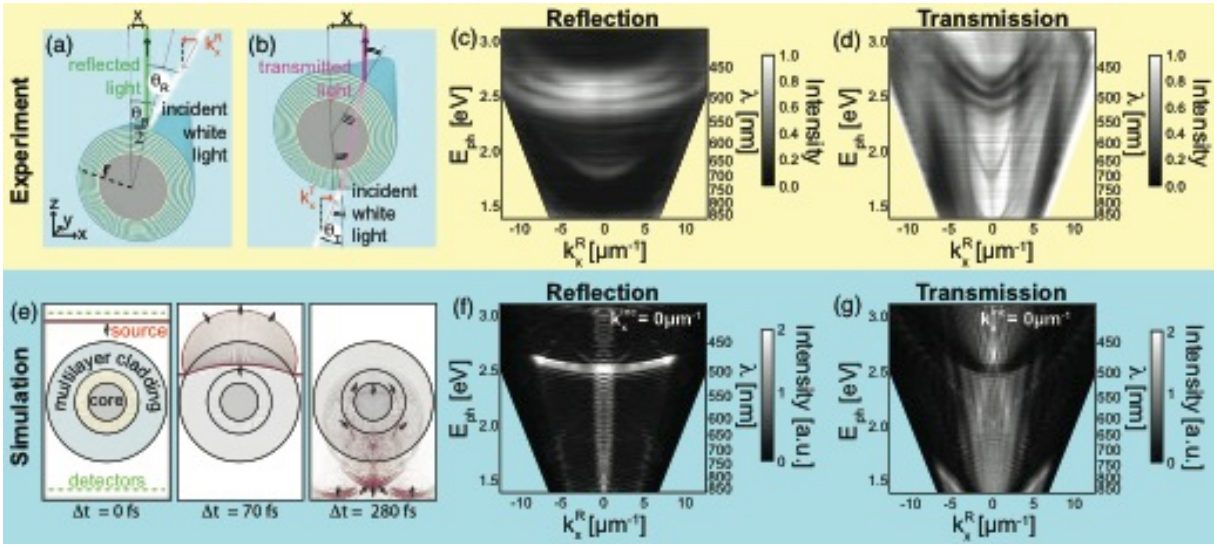

Figure 3: Comparison of optical modeling with experimental data. (a) Simplified schematic representation of light reflection from the fiber into the vertical direction, revealing the relation between projected radial distance x from the multilayer fiber symmetry axis and the angle of light incidence θ_R (effects induced by the finite numerical aperture of illumination

and collection optics, including extended light cones have been neglected in this sketch). (b) A similar schematic for light transversely transmitted by the fiber. (c) Band diagram of the fiber reflection for light in the visible range. (d) Band diagram of the fiber transmission. (e) The left image visualizes the FDTD simulation cell set-up used for optical modeling, including the cross-section of the fiber with an inner cladding periodicity of 710nm (yellow) and an outer periodicity of 340nm (light blue), the incident light pulse spanning the whole visible range (red and blue), the reflection and transmission detectors (green dashed lines) and absorbing boundaries at the cell edges (black). The following two images show the light pulse propagating transversely through the multilayer fiber at two later points in time and for clarity, the fiber is shown in its contours. In all three images the logarithm of the light pulse's field amplitudes is shown increasing in value from blue to red. (f, g) Reflection and transmission band diagrams deduced from the simulations for perpendicular light incidence ($k_x = 0$ m^{-1}).

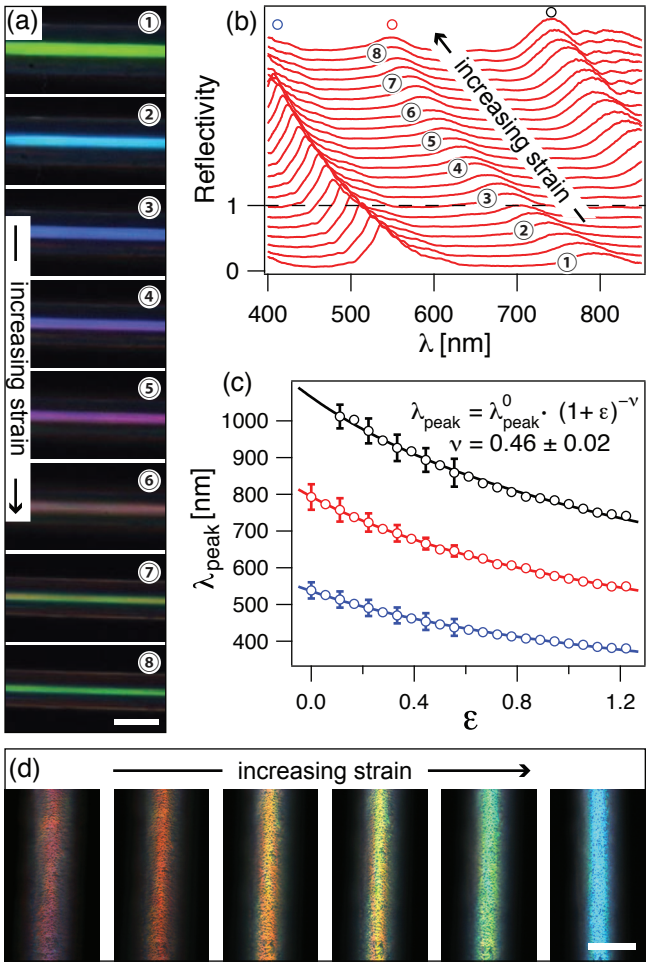

Figure 4: Mechanical tuning of the fibers' optical performance: (a) Optical micrographs of a fully elastic fiber showing the color tuning upon mechanical deformation induced by elongation along the fiber axis. The stiff glass core was removed from the fiber by pullout. Scale bar 50µm. (b) The corresponding variation in the reflection spectrum. The bottom spectrum is shown on absolute scale (this particular fiber showed a peak reflectivity of over 70%) and subsequent spectra are offset from the previous one by 0.15. The numbers correspond to the numbered micrographs in (a). (c) Variation of peak wavelength λ_{peak} with applied strain ε. The open circles of different color correspond to three observed reflection peaks (labeled in (b) with corresponding open circles). The lines represent fits based on a power law that results from considering the fiber to be isotropically elastic, with the fit parameter ν representing the fiber's Poisson's ratio. The error bars shown for a selection of data points correspond to the standard deviation of the peak positions obtained for five consecutive stretch runs at different positions along the fiber. (d) Color tuning of a second fiber with different layer thickness where the glass core was removed by a hydrofluoric acid etch. The fiber color can be tuned throughout the whole visible spectrum. The dark spots on the fiber result from scattering caused by etching artifacts found in at least the top PDMS film in the multilayer cladding, which is also affected by the hydrofluoric acid. Scale bar 50µm.

Supporting Information:

Variations in fiber geometry

Small modifications in the process of rolling the multilayer cladding onto the core fiber permit the realization of different internal geometries in the fiber. Attachment of the core fiber at the end of a free floating bilayer results in a fiber with one periodicity throughout the whole cladding (Fig. S1a). By attaching the core fiber a certain offset distance away from the edge of the bilayer film, claddings with two distinct multilayer periodicities can be realized (Fig. S1b). In this case, the inner section of the multilayer cladding has twice the periodicity of the outer section and the ratio of layer numbers in the inner and outer section can be controlled by controlling the distance between bilayer edge and fiber attachment line. Chirped multilayer claddings with a gradient in periodicity are realized by fixing the distance between the core fiber and the far edge of the bilayer during rolling leading to a successive stretching of the bilayer and a corresponding thinning of the rolled-up layers. As expected, such chirped multilayer fibers have a silvery appearance due to a wide reflection band.

Extraction of band-diagrams from experimental data

The band diagrams presented in the article were acquired from a fiber with two distinct periodicities in the cladding, the periodicity of the inner layers being about twice the periodicity of the outer layers which amounted to (350 ± 20) nm. The number of layers with double periodicity in the inner cladding zone is determined by the distance of the attachment line of the core fiber from the edge of the initial bilayer prior to the rolling (see Fig. S1b). The reflection and transmission data collected from the fiber in spatially resolved reflection and transmission intensity mappings (Fig.S2a) serve as the starting point for the extraction of the fiber's band-diagrams. The in-plane wave-vector k_x and the incidence angle θ of the incident light collected after reflection or transmission are directly related to the ratio $\bar{x} = {}^{x}/_{r}$ between

the fractional lateral distance x of the emerging ray from the axis of the fiber and its radius r (Fig. S2b). Taking into account the fiber geometry and the directionality of light detection this in-plane wave vector component k_x^R of the incident light collected after reflection is defined by $k_x^R = k_0 \sin(\theta_R) = k_0 \sin(2sin^{-1}(\bar{x}))$, where $k_0 = {}^{2\pi}/_{\lambda}$, λ is the wavelength and θ_R is the incidence angle of the reflected light (Fig. S2b, top). The in-plane wave vector component k_x^T of incident light transmitted transversely through the fibre (Fig. S2b, bottom) is defined by $k_x^R = k_0 \sin(\theta_R) = k_0 \sin(2\,(sin^{-1}(\bar{x}) - \sin^{-1}({}^{\bar{x}}/_{n_{eff}})))$, where θ_T is the incidence angle of the collected transmitted light and n_{eff} is the effective refractive index of the fiber, approximately given by $n_{eff} \approx \sqrt{\frac{n_1^2 d_1 + n_2^2 d_2}{d_1 + d_2}}$ with $n_{1,2}$, $d_{1,2}$ being the refractive indices and thicknesses of the constituent layers.

The resulting dispersion relations are plotted in Fig. S2c against the in-plane wave vector k_x of the incident light. To account for the limited numerical aperture of the illumination and collection optics in the micro-spectroscope the band diagrams have to be corrected by the optical transfer function (OTF) of the setup. The OTF is given by the overlap of numerical aperture of the collection optics and the light cone emerging from the fiber surface at an angle θ after reflection or transmission (Fig. S2d).[1] This is schematically represented in Fig. S2d for reflection (top) and transmission (bottom). The overlap area defining the OTF is shown in green. The numerical apertures in these schematics are not drawn to scale. In the reflection measurements the illumination and collection is achieved via the same 50x objective with a numerical aperture of 0.55 resulting in the optical transfer function plotted in Fig. S2d (blue line) against the angle θ between incident and emerging light cone, which is determined by the orientation of the fibre surface at the collection point. In the transmission measurements a condenser with a numerical aperture of 0.9 was used. The resulting band-diagrams after correction for the OTF of the setup are shown in Fig. S2e).

Guided modes in the fiber cladding

Finite Difference Time Domain simulations employing the freely available software package MEEP[2] were carried out to identify the origin of an additional mode found in the transmission band-diagram in the range around 2eV to 2.5eV. Simulations of the reflection and transmission of a fiber with single periodicity show that this mode only exists for perpendicularly polarized light, i.e. light with its electric field vector aligned with the fiber axis (Fig. S3a). Monitoring the total energy in the simulation cell during the length of the simulation reveals the differences between the two orthogonal polarizations (Fig. S3b). The features in the decay of energy over time for both polarizations in the simulation cell can clearly be matched to specific events during the simulation visualized by representing field distributions (on log scale) at given times (Fig. S3c, numbers in the images correspond to numbers in (b)). Abrupt decays of total energy in the cell early on in the simulation relate to the exit of reflected waves at the top boundary (Fig. S3c 1,2) and scattering of waves that subsequently leave at the side walls (Fig. S3b 4,5). Significant differences between the two polarization states are the manifestation of the Brewster effect for parallel-polarized light (Fig. S3c 1, bottom) and the proportionally stronger scattering of perpendicularly polarized light (Fig. S3c 3,4). As a consequence, proportionally more parallel-polarized light is transmitted through the fiber. The most significant decay in total energy in the simulation cell results from the exit of waves after transmission through the fiber at the lower simulation cell boundary (Fig. S3c 5,6). That decay is proportionally more pronounced for the parallel-polarized light component. This difference resulting from the Brewster effect sets the differences in the transmission distributions of the two light polarizations at higher in-plane wave vector component k_x. After exit of the majority of light in transmission from both polarisation states a significantly higher total energy remains in the cell for perpendicularly polarized light resulting from the coupling of waves into guided modes in the fiber cladding (compare (Fig.

S3c 5,6 top with 5,6 bottom). This guiding in the cladding, which is more effective in confining light with perpendicular field vector is the origin for the mode that is observed only in transmission.

[1] J.W. Goodman, *Introduction to Fourier Optics*, Roberts and Company Publishers, Greenwood Village, USA, **2005**.

[2] A. F. Oskooi, D. Roundy, M. Ibanescu, P. Bermel, J. D. Joannopoulos, S. G. Johnson, *Computer Physics Communications* **2010**, *181*, 687.

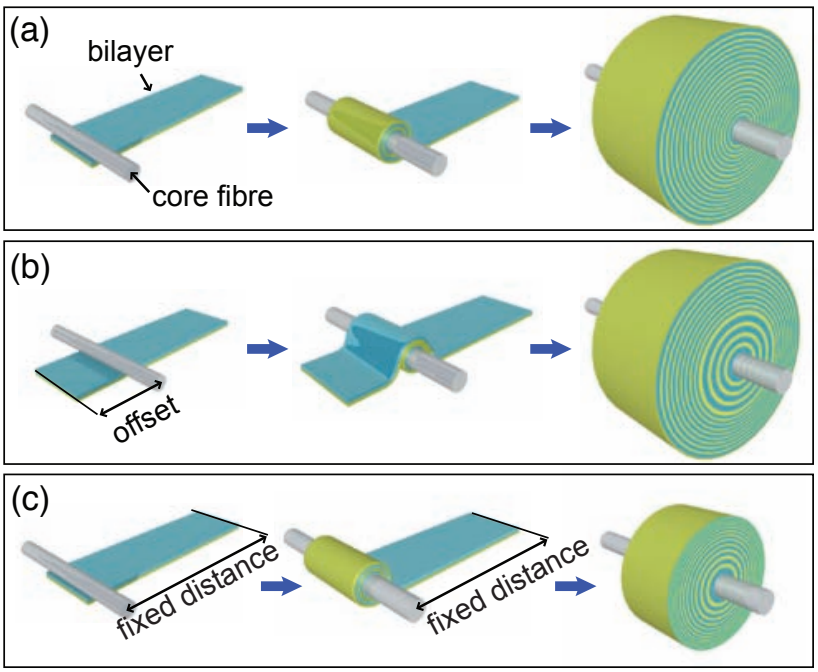

Figure S1: Fiber-internal geometries. A set of simple internal geometries can be achieved by small modifications of the manufacturing procedure. (a) Rolling of fibres with a single periodicity. (b) Realization of fibers with two internal periodicities. (c) Rolling of fibers with gradual thickness variation.

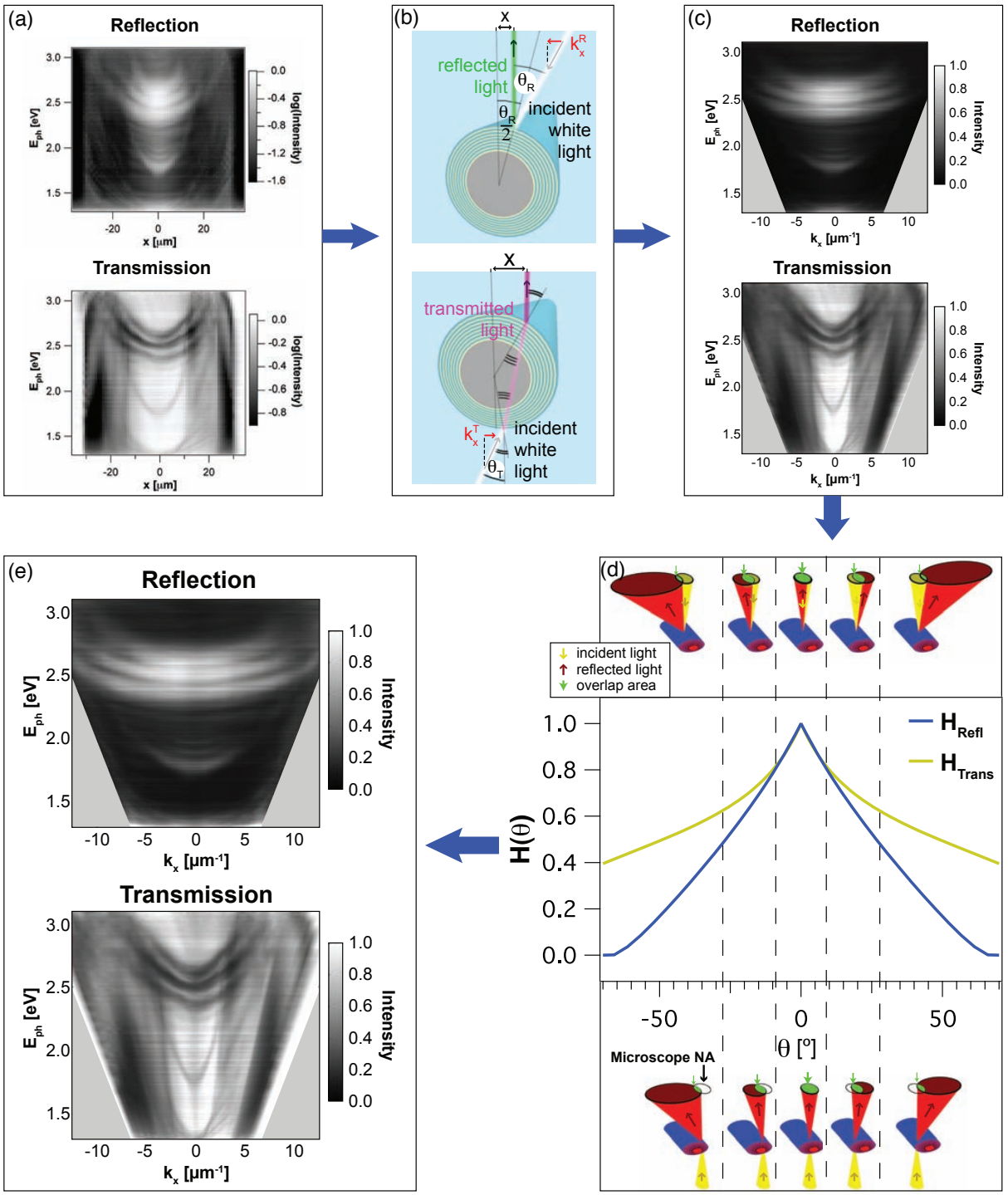

Figure S2: Deduction of band diagrams from radial intensity distributions of fiber transmission and reflection. (a) The original data acquired by micro-spectroscopy showing the radial intensity distribution of fiber reflection and transmission. (b) Schematic representation of the geometrical relations between measured radial projected distance x and light incidence angle $\theta_{R,T}$ for reflection and transmission. (c) Data deduced by taking into account the relation between x and $\theta_{R,T}$. Optical transfer function of the microscope $H(\theta_{R,T})$ for measurements in transmission (yellow) and reflection (blue). Simplified schematic illustrations of the origin of the setup's optical transfer function as the overlap (green intersection) between reflected light (top row) or transmitted (bottom row) light. The numerical aperture of condenser and objective are not drawn to scale (d) Reflection and transmission band-diagrams after all corrections are applied.

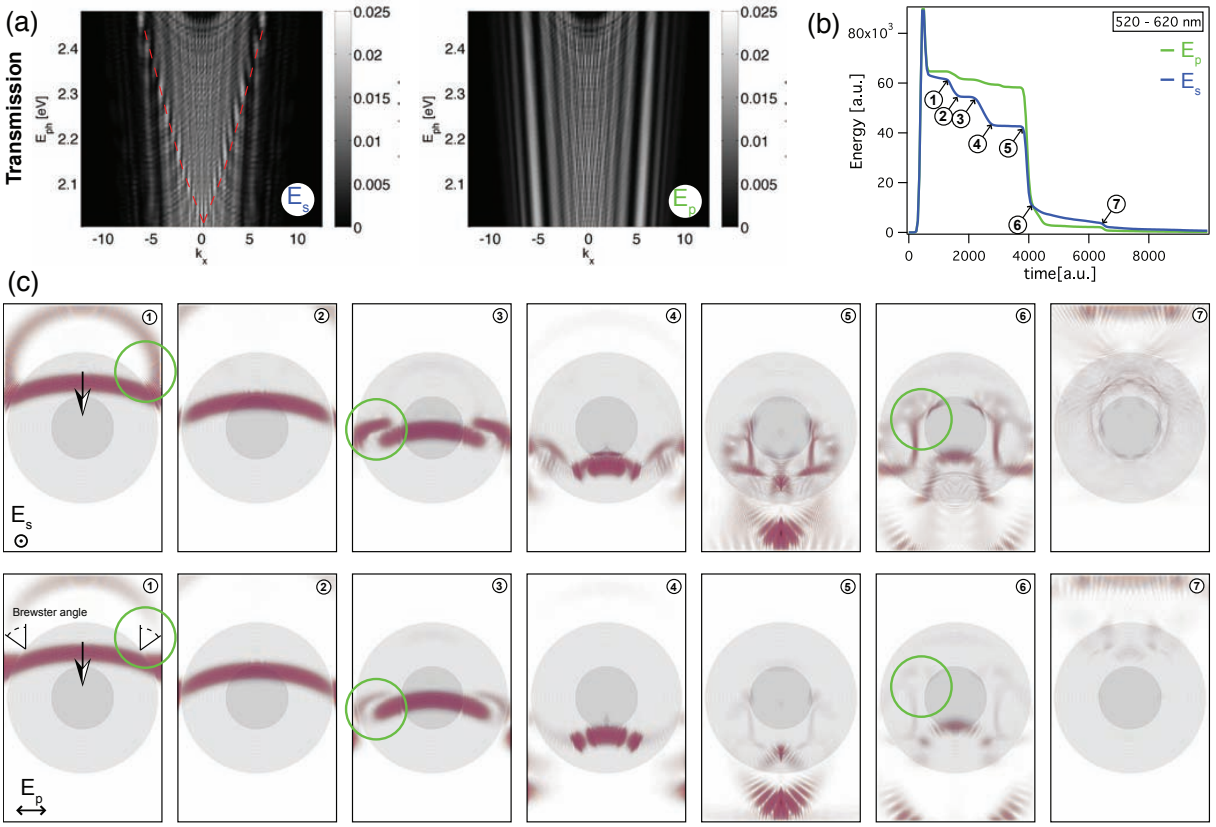

Figure S3: Polarization dependent guiding of light in the fiber cladding. (a) Simulated transmission band-diagrams for perpendicular (E_s) and parallel (E_p) polarised light in the range of 2eV - 2.5eV for a fibre of 340nm cladding periodicity. The red dashed light in the transmission band-diagram underlines the presence of a guided mode for perpendicularly polarized light. (b) Total energy decay in the simulation cell as a function of simulation time for parallel and perpendicularly polarized light. The numbers mark different pathways of energy leaving the cell. (1)(2) - reflected light leaving at the upper boundary, (3)(4) - scattered waves leaving the cell at the sidewalls, (5)(6) transmitted waves exiting at the lower boundary, (7) - waves leaving at the upper boundary after incurring internal reflection within the fiber. (c) Color-coded representation of the logarithm of the field distribution of perpendicularly (top) and parallel (bottom) polarized light for the time points enumerated in (b). Green circles point out the differences between the two polarization states.